Advances in Geo-Energy Research

Vol. 8, No. 3, p. 181-192, 2023

Original article

Simulation of the effect of stand-off parameter on collapse behaviours of a single cavitation bubble in jet drilling

Xiaoya Wu[1], Yiqun Zhang[2,3]*, Haochen Huang[1], Chengyu Hui[2], Zhaowen Hu[2], Gensheng Li[1,3]

[1]*College of Petroleum Engineering, China University of Petroleum, Beijing 102249, P. R. China*

[2]*College of Safety and Ocean Engineering, China University of Petroleum, Beijing 102249, P. R. China*

[3]*State Key Laboratory of Natural Gas Hydrate, China University of Petroleum, Beijing 102249, P. R. China*

Keywords:
Cavitation bubble
stand-off parameter
bubble collapse
shock wave
micro jet

Cited as:
Wu, X., Zhang, Y., Huang, H., Hui, C., Hu, Z., Li, G. Simulation of the effect of stand-off parameter on collapse behaviours of a single cavitation bubble in jet drilling. Advances in Geo-Energy Research, 2023, 8(3): 181-192.
https://doi.org/10.46690/ager.2023.06.05

Abstract:
Cavitation jet drilling has been extensively employed for the exploitation of geo-energy resources. The dynamics of cavitation bubbles in close proximity to the solid boundary have been a subject of great interest during jet drilling, as they play a crucial role in determining the cavitation performance. In present work, the dynamics of a single cavitation bubble near a solid surface is numerically investigated by using the axisymmetric Navier-Stokes equations and the volume of fluid method with considering the surface tension of gas-liquid interface, liquid viscosity and compressibility of gas in bubble. The simulated profiles are qualitatively and quantitatively consistent with the experimental images, which proves the reliability of employed numerical model. The effects of stand-off distance on the bubble profiles, bubble volume and collapse time have been analysed. Moreover, the cavitation erosion patterns towards the solid wall are also revealed for different dimensionless stand-off distances. The simulation results reveal two distinct collapse patterns for the bubble profiles. The solid wall significantly impedes the shrinkage rate of the bubble, resulting in the longest collapse time when the dimensionless stand-off distance is 1.0. Three erosion patterns of cavitation bubbles towards the solid wall are observed, with the shock wave and micro-jet both contributing significantly to the damage caused by cavitation erosion. The shock wave sweeps the wall resulting in circular corrosion pits with a severely eroded centre, while the micro jet penetrates the wall leading to small spot corrosion pits.

1. Introduction

Cavitation refers to the formation of vapor bubbles in a liquid due to a decrease in local pressure below the saturated vapor pressure. The collapse of these cavitation bubbles releases instantaneous high pressure and high temperature (Xu et al., 2021). This phenomenon is known to cause severe erosion on various components such as warship propellers, hydraulic pumps, and turbines (Cui et al., 2022). Despite being undesirable in many engineering situations, cavitation bubbles have been actively harnessed by certain technologies due to the tremendous energy they release. Cavitation jet can be adopted for pipeline cleaning (Peng et al., 2018; Bukharin et al., 2020), drilling rate improvement (Li et al., 2005; Wu et al., 2022) and metals peening (Soyama et al., 2011). At present, a large resource of methane hydrates has been explored beneath the seabed (Cui et al., 2018; Shaibu et al., 2021), and the exploitation method using jet breaking technology gains much attention (Wang et al., 2018; Zhou et al., 2018; Huang et al., 2023). An innovative recovery method is proposed by Li et al. (2020) for the exploitation of natural gas hydrates, and the cavitation jet is selected as the critical technology due to its strong cavitation erosion ability (Zhang et al., 2022). Fig. 1 shows the schematic of cavitation jet drilling rocks. As shown in Fig. 1, the jet flows through the resonator and generates large-scale vortex rings. The low-pressure region located at the vortex cores guarantees the initiation and development. The generated cavitation bubbles flow with water during the jet erosion process and then experience expansion when liquid

Yandy Scientific Press

*Corresponding author.
E-mail address: 15611563215@163.com (X. Wu); zhangyq@cup.edu.cn (Y. Zhang); huanghaochen@student.cup.edu.cn (H. Huang); 2021310512@student.cup.edu.cn (C. Hui); hu_zhaowen@163.com (Z. Hu); ligs@cup.edu.cn (G. Li).

Received May 10, 2023; revised June 01, 2023; accepted June 14, 2023; available online June 16, 2023.

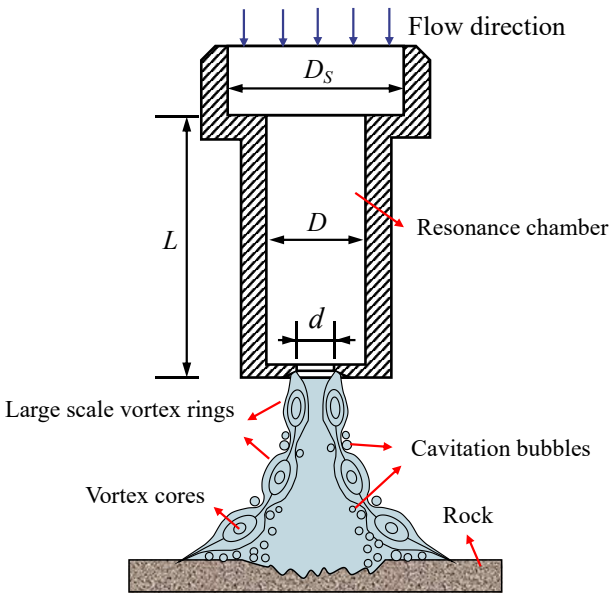

Fig. 1. Schematic of cavitation jet drilling rocks: D_s-diameter of inlet pipe, D-diameter of resonance chamber, d-nozzle diameter, and L-length of resonance chamber.

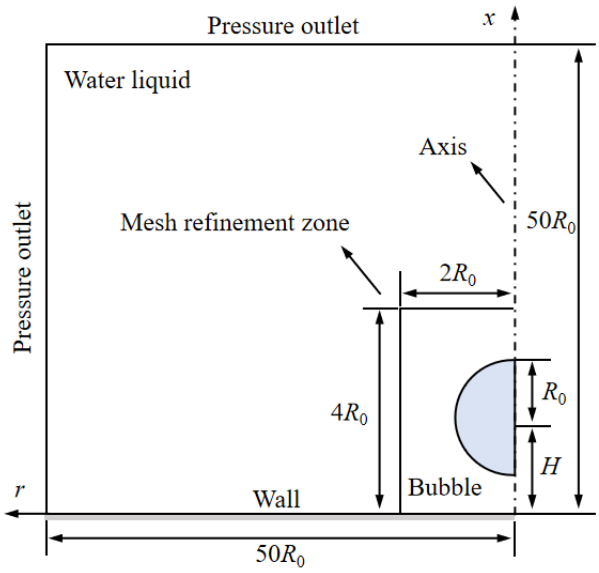

Fig. 2. Schematic diagram of the computational domain.

pressure declines gradually (Peng et al., 2018). After reaching the rock surface, the local pressure of the liquid recovers. Then the cavitation bubbles collapse near the rock surface and cause cavitation damage. Therefore, exploring the collapse process of cavitation bubbles near the rigid wall is conducive to the utilization of cavitation energy.

Numerous numerical and experimental investigations have been conducted to study the dynamic behaviours of cavitation bubbles. Rayleigh (1917) conducted the first systematic study on bubble dynamics and developed a theoretical model that describes the growth and collapse of spherical bubbles in an infinite domain. Plesset (1949) extended this work by considering the effects of surface tension, resulting in simulated results that align well with experimental data. The stand-off distance, characterized by the ratio of the distance between the initial bubble centre and the wall to the maximum bubble radius, is commonly denoted as the stand-off parameter γ. Brujan and Matsumoto (2012) experimentally examined the distance dependence between the bubble and the wall and observed a significant impact of the stand-off parameter on jet penetration velocity and shock wave pressure. These quantities exhibit a minimum at $\gamma = 1$ and remain constant for $\gamma > 3$. Xia et al. (2018) investigated the influence of γ on the collapse behaviours of individual cavitation bubbles, revealing that the cavitation erosion mechanism on the solid wall is notably determined by γ. Furthermore, the area swept by the shock wave is relatively wider for $\gamma = 2$. Yin et al. (2021) focused on the dynamics of rebound bubbles and their multi-period evolutions near rigid boundaries, highlighting the significant influence of the dimensionless stand-off distance γ on pressure peaks and maximum temperature.

Previous researches have indicated the significant impact of the stand-off distance on shock waves and resultant micro-jet, yet the cavitation erosion mechanisms on the solid wall remain poorly understood. This study focuses on computing the evolution of bubble profiles as a function of the stand-off distance. It analyses the effects of the stand-off distance on bubble volume and collapse time. Additionally, it unveils the cavitation erosion patterns towards the solid wall for varying stand-off distances.

2. Methodology for simulation

2.1 Computational domain

Fig. 2 depicts the schematic of the computational domain used in the simulation. The bubble collapse is assumed to be axisymmetric, utilizing a two-dimensional axisymmetric coordinate system. The axial and radial coordinates are denoted by x and r, respectively. The bottom boundary enforces a non-slip wall condition, whereas the left and upper boundaries apply pressure outlet conditions. The centerline follows an axis condition. The initial radius of the cavitation bubble is labeled as R_0. H denotes the distance between the center of bubble and the bottom wall. To mitigate boundary effects on the simulation results, a model size of $50R_0 \times 50R_0$ is chosen, and quadrilateral cells are used to mesh the entire domain. A mesh refinement zone, with dimensions of $2R_0 \times 4R_0$, is arranged around the cavitation bubble to accurately capture its motion. The nondimensional stand-off distance, γ, is introduced and defined as the ratio of H to R_0.

2.2 Governing equations

The mass conservation equation for the mixture is:

$$\frac{\partial \rho_m}{\partial \rho_t} + \nabla \cdot \rho_m v = 0 \tag{1}$$

where ρ_m is the mixture density, t is time, and v is the velocity vector.

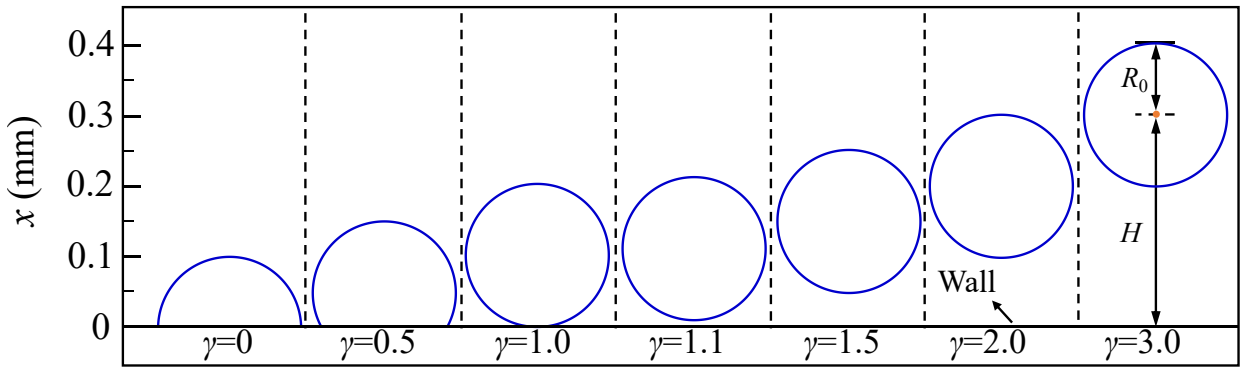

Fig. 3. Schematic of cavitation bubbles near the solid wall with different γ ($\gamma = H/R_0$).

The momentum equation is:

$$\frac{\partial}{\partial t}(\rho_m v) + \nabla(\rho_m v v) = -\nabla p + \nabla\left[\mu_m\left(\nabla v + \nabla v^T\right) - \frac{2}{3}\mu_m \nabla \cdot vI\right] + F_\sigma \tag{2}$$

where p is fluid pressure, μ_m is the dynamic viscosity, and I represents the unit tensor.

F_σ denotes the surface tension term, calculated by the CSF model (Brackbill et al., 1992):

$$\begin{cases} F_\sigma = \sigma \dfrac{\rho_m \kappa \nabla \alpha_l}{0.5(\rho_g + \rho_l)} \\ \kappa = \nabla \cdot \dfrac{n}{|n|} \end{cases} \tag{3}$$

where the surface tension coefficient σ has a value of 0.0725 N/m. κ represents the curvature of the phases interface. ρ_g and ρ_l are respectively the densities of gas and liquid. n represents the surface normal, which is determined by the gradient of the liquid-phase volume fraction α_1.

The energy equation is:

$$\frac{\partial(\rho_m E)}{\partial t} + \nabla \cdot (v(\rho_m + p)) = \nabla \cdot \left(k \nabla T_f\right) \tag{4}$$

where E is the total energy calculated using Eq. (5). k denotes the thermal conductivity, and T_f represents the liquid temperature:

$$E = \frac{\alpha_g \rho_g E_g + \alpha_l \rho_l E_l}{\alpha_g \rho_g + \alpha_l \rho_l} \tag{5}$$

where α_g is the volume fraction of gas. E_g and E_l are respectively the gas energy and liquid energy.

The volume of fluid method (Hirt and Nichols, 1981) is employed to capture the bubble profile. The evolution of the liquid volume fraction is given as:

$$\frac{\partial \alpha_l}{\partial_t} + v \cdot \nabla \alpha_l = 0 \tag{6}$$

And the α_g is solved using:

$$\alpha_l + \alpha_g = 1 \tag{7}$$

The calculation principles of density and viscosity can be formulated as:

$$\begin{cases} \rho_m = \rho_l \alpha_l + \rho_g \alpha_g \\ \mu_m = \mu_l \alpha_l + \mu_g \alpha_g \end{cases} \tag{8}$$

The vapor density changes in accordance with the ideal gas law, as follows:

$$\rho_g = \frac{p M_w}{R T_f} \tag{9}$$

where M_w is the gas molecular weight, and R is the gas constant.

2.3 Solution strategy

The pressure outlet boundary is subjected to a pressure of 0.1 MPa. The initial vapor pressure within the bubble is defined as the saturated vapor pressure of water at 300 K, which is 3,568 Pa, utilizing the calculation principle derived from the Antoine equation (Thomson, 1946). Two types of bubbles, namely those on the solid wall and those near the solid wall, are distinguished based on the parameter γ. Three cases are simulated for bubbles on the bottom wall, corresponding to γ values of 0, 0.5, and 1.0. In the case of bubbles near the bottom wall, four different γ values are used: 1.1, 1.5, 2.0, and 3.0. The schematic of bubbles with different γ values is shown in Fig. 3.

In the simulation, the pressure implicit with splitting of operators scheme (Issa, 1986) is utilized for solving the pressure-velocity coupling in the flows. The pressure staggering option scheme (Baliga and Patankar, 1980) is used to compute the pressure. The geometric reconstruction scheme (Youngs, 1984) is employed to solve the volume fraction equation. A residual convergence criterion of 10^{-6} is set for both mass and momentum conservation, and a residual convergence criterion of 10^{-9} is set for the energy conservation equation. Furthermore, a variable time step method ranging from 1×10^{-11} to 1×10^{-9} s is implemented for the transient simulation to enhance computational efficiency.

3. Model validation

The mesh size is crucial for tracking the bubble dynamics. For the validation of model, the cell number per bubble radius (CPBR) parameter (Mohammad and Ehsan, 2008) is adopted to characterize the mesh size. A grid independence study is conducted for the mesh refinement zone using three CPBR values of 50, 100, and 200. The corresponding mesh sizes are 2 μm × 2 μm, 1 μm × 1 μm and 0.5 μm × 0.5 μm. Simulation results indicate that the maximum deviation is less than 1% as CPBR increases from 100 to 200, indicating that the mesh size

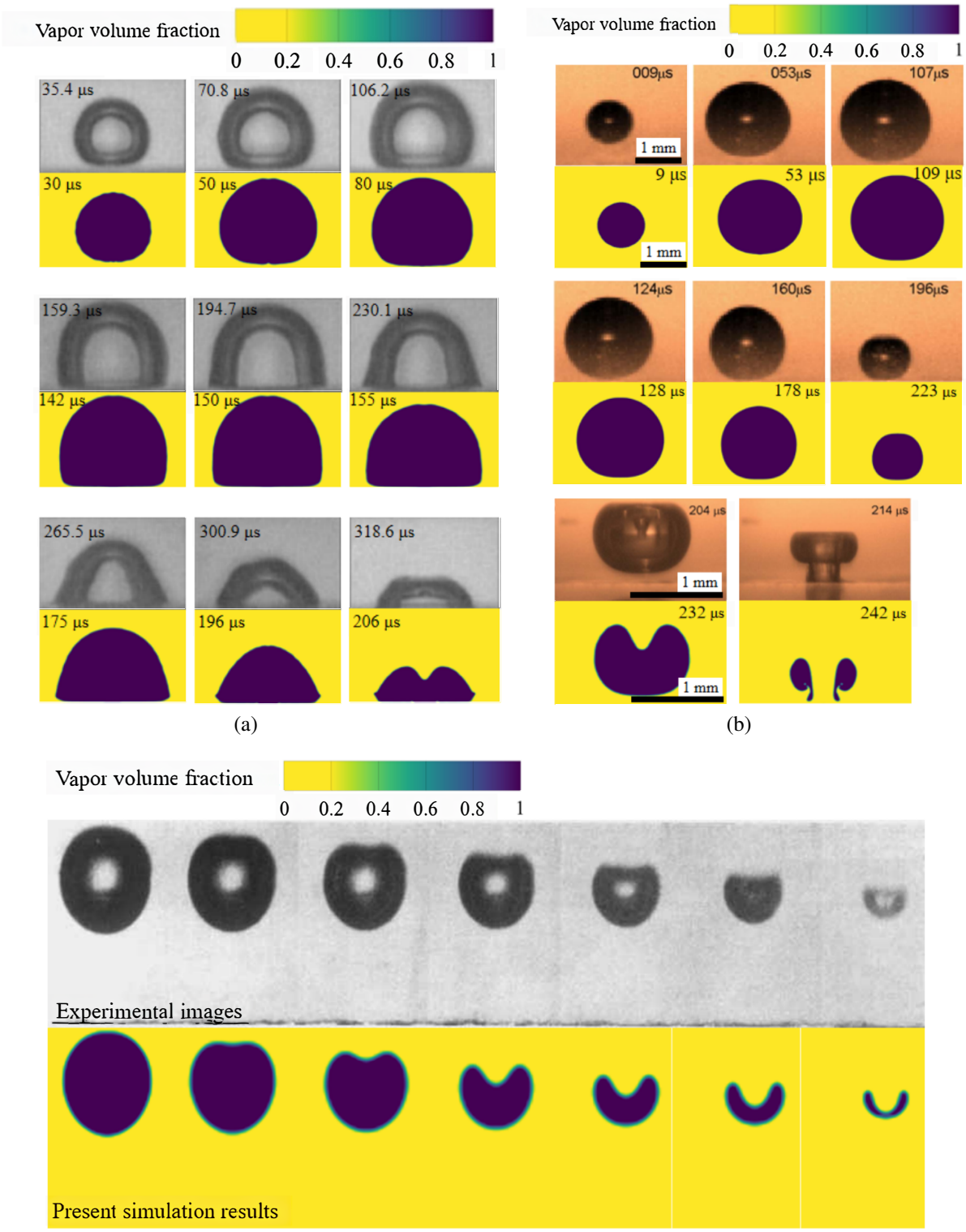

Fig. 4. The comparison between experimental images and simulated bubble profiles for (a) γ = 0.6, (b) γ = 1.0 and (c) γ = 1.5.

has little influence on the numerical model in this scenario. A CPBR value of 100 is chosen for all simulations, which not only ensures calculation efficiency but also maintains accuracy.

The numerical model is validated by comparing the simulated cavitation bubble profiles to experimental images from previous literature for three different values of γ. Figs. 4(a)

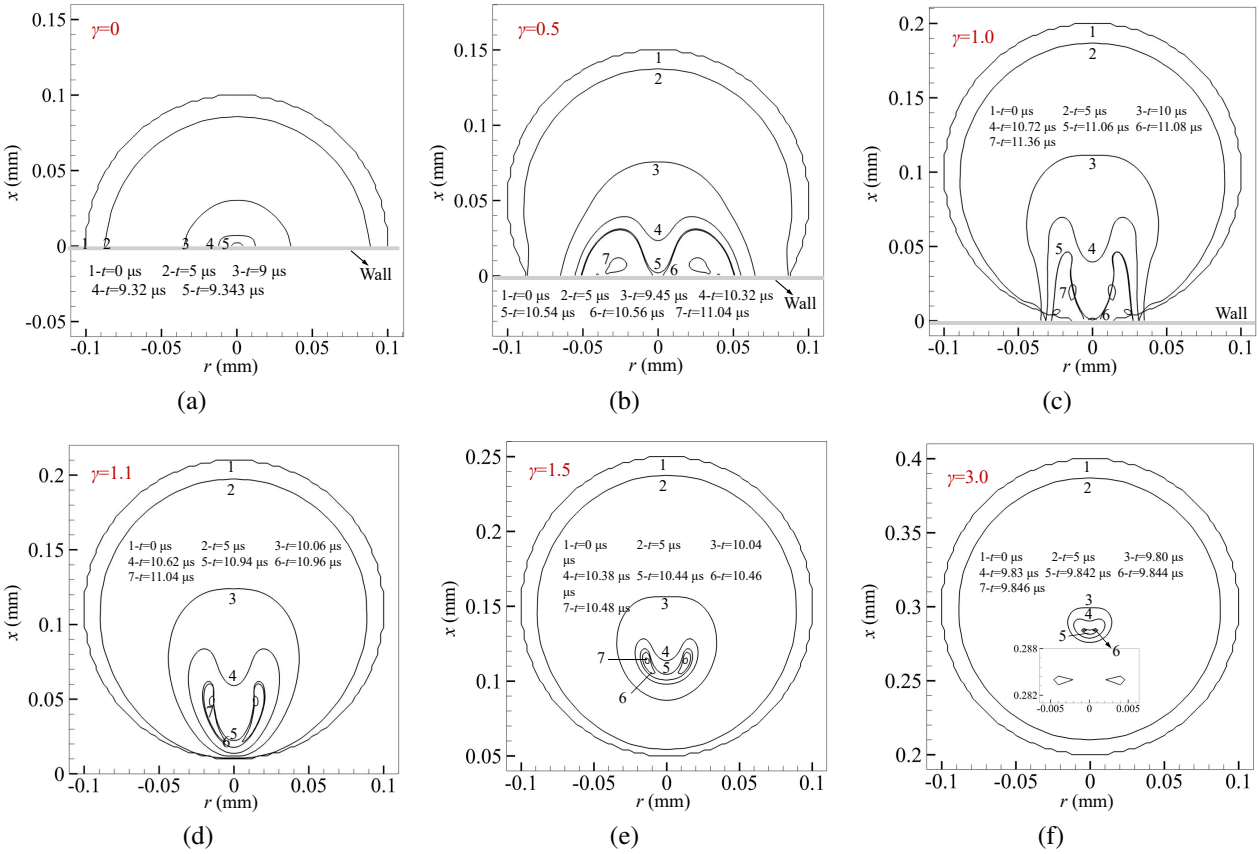

Fig. 5. Bubble profiles for different γ: (a) γ = 0, (b) γ = 0.5, (c) γ = 1.0, (d) γ = 1.1, (e) γ = 1.5 and (f) γ = 3.0.

and 4(b) present a comparison between the experimental images and simulated profiles of attached bubbles for γ values of 0.6 and 1.0, respectively. The experimental data and initial conditions of the numerical model are obtained from previous studies (Philipp and Lauterborn, 1998; Ohl et al., 2006; Minsier et al., 2009). In both Figs. 4(a) and 4(b), the experimental bubble profiles are in good agreement with the simulated bubble profiles. Fig. 4(c) shows a comparison between the experimental images and simulated profiles of detached bubbles for γ = 1.5. The experimental data are taken from previous work (Lauterborn and Bolle, 1975). The evolutions of bubble profiles simulated agree well with that of the experimental images. In conclusion, the present model is credible.

4. Results and discussion

4.1 Evolutions of bubble profiles

Fig. 5 shows the bubble profiles, determined by the vapor volume fraction of 0.5 at typical moments for various γ values. The bubble shapes at different γ values are influenced to varying degrees by the presence of the solid wall. To facilitate analysis, specific critical moments, referred to as moment 1 to moment 7, are chosen. However, this selection is not applicable for the case of γ = 0 in Fig. 5(a). Moment 1 corresponds to the bubble's initial state, while moment 2 signifies the transition period when the bubble profile steadily contracts under ambient pressure. Subsequently, the upper bubble interface flattens due to the asymmetrical collapse, as observed in all cases. This state is labelled as moment 3. Following that, water penetrates the bubble, forming a jet and causing the upper part of the interface to become concave. This phenomenon is referred to as moment 4. However, this phenomenon is absent throughout the entire collapse process for the case of γ = 0 in Fig. 5(a). Moment 5 demonstrates the upper bubble interface moving closer to the lower part of the bubble profile. Jet formation concludes when the liquid completely penetrates the bubble profile, resulting in direct impact on the bottom wall, as depicted in moment 6. Subsequently, the bubble assumes a toroidal shape, and under the influence of ambient pressure, it continues to shrink, as illustrated in moment 7. It is important to note that a micro-jet does not form in Fig. 5(a). Throughout the entire collapse process, the bubble profile only undergoes shrinkage, maintaining a hemispherical shape. Overall, based on the aforementioned analysis, it can be deduced that there are two distinct collapse patterns for cavitation bubble profiles as γ ranges from 0 to 3.0, as depicted in Figs. 5(a)-5(f). In Fig. 5(a), when γ = 0, the bubble profile consistently retains a hemispherical shape and ultimately collapses under ambient pressure. Conversely, in Figs. 5(b)-5(f), as γ ranges from 0.5 to 3.0, the entire process includes the jet penetration stage and the collapse stage.

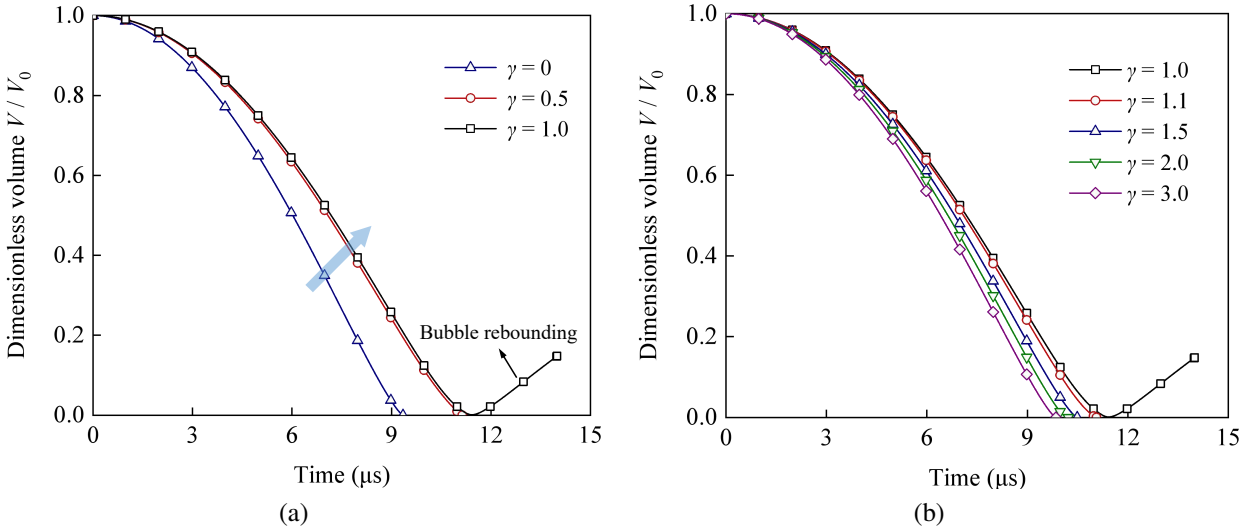

Fig. 6. The ratio of V/V_0 for different γ: (a) $0 \leq \gamma \leq 1.0$ and (b) $1.0 \leq \gamma \leq 3.0$.

4.2 Bubble volume and collapse time

The evolution of bubble profiles is significantly influenced by the solid wall, as described in Section 4.1. Fig. 5 illustrates that the volume change between two identical moments varies for different γ values. Fig. 6 presents the ratio of the bubble volume to its initial state (V/V_0) for γ values ranging from 0 to 3.0. Here, V_0 represents the maximum volume of the bubble.

Figs. 6(a) and 6(b) reveal that the bubble volume experiences a slight reduction due to the relatively slow compression of the external fluid at the initial moment. Following that, the compression velocity progressively intensifies under the influence of ambient pressure, resulting in an accelerated shrinkage. Eventually, the compression velocity decreases, leading to a decline in the rate of bubble shrinkage. These characteristics are consistent among cavitation bubbles with varying γ values. For comparison, the cavitation bubble at $\gamma = 1$ is selected as the reference sample. In Fig. 6(a), it is evident that increasing γ decreases the rate of bubble shrinkage, accompanied by a noticeable delay in the collapse time within the range of $0 \leq \gamma \leq 1.0$. Conversely, in Fig. 6(b), increasing γ leads to a reduction in the bubble volume and decreases the collapse time with γ varying from 1.0 to 3.0. Furthermore, at $\gamma = 1$, the bubble exhibits a distinct small rebound at the conclusion of the collapse process.

Fig. 7(a) presents the dimensionless volume of the bubble for various γ values at moment 3 and moment 6. Moment 3 represents the state where the upper part of the bubble flattens, while moment 6 represents the state where the jet penetrates the bubble completely. The dimensionless volume at moment 3 and moment 6 gradually decreases with increasing γ, suggesting a tendency toward symmetrical bubble collapse and an increase in compressing velocity with higher γ values. As the bubble detaches from the surface, the compressed volume at moment 6 steadily increases, facilitating the formation of a high-velocity jet. Fig. 7(b) illustrates the collected collapse times of cavitation bubbles at different γ values. The collapse time initially increases and then decreases as γ ranges from 0 to 3.0, reaching its maximum at $\gamma = 1.0$. The analysis reveals that for cavitation bubbles on the wall ($\gamma \leq 1$), the initial bubble volume affects the collapse time more. A smaller γ implies a smaller initial bubble volume and, therefore, a shorter collapse time. On the other hand, for cavitation bubbles near the solid wall ($\gamma \geq 1$), the solid wall has a stronger influence on the collapse time. As γ increases, the blocking effect from the rigid wall on the lower bubble interface weakens, leading to an increase in compressing velocity. Consequently, the collapse time gradually decreases. When $\gamma \geq 1$, the collapse time approaches a critical value of 9.314 μs, calculated using Eq. (10), which corresponds to the scenario of an infinite cavitation bubble:

$$t_c = 0.91468 R_0 \sqrt{\frac{\rho_l}{p_{out} - p_{in}}} \tag{10}$$

where t_c is the collapse time, and R_0 is the bubble radius, p_{in} and p_{out} respectively represent the bubble pressure and environmental pressure.

4.3 Cavitation erosion patterns

This section analyses the pressure and velocity fields at different γ values. The temporal evolution of pressure at the centre of the wall is recorded and presented in Fig. 8. Previous studies have identified the cavitation erosion mechanisms on a solid wall as shock waves (Kornfeld and Suvorov, 1944) and micro-jets (Rayleigh, 1917). Building on this knowledge, a detailed analysis of the cavitation erosion pattern under different γ values are conducted, utilizing pressure evaluations, velocity vectors, and bubble profiles over time for illustration purposes.

The pressure undergoes significant changes over time due to the movement of the bubble profile, particularly during moments of jet penetration into the bubble and bubble collapse. Therefore, the focus is primarily on the peak pressures for different γ values to interpret the cavitation erosion pattern.

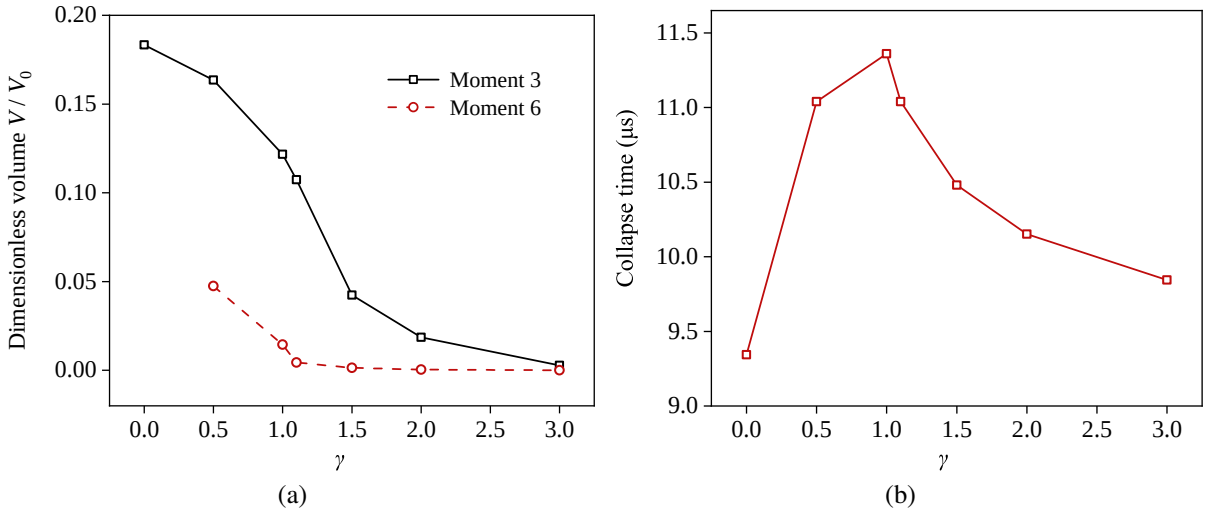

Fig. 7. The (a) bubble volume and (b) collapse time of bubbles for various γ.

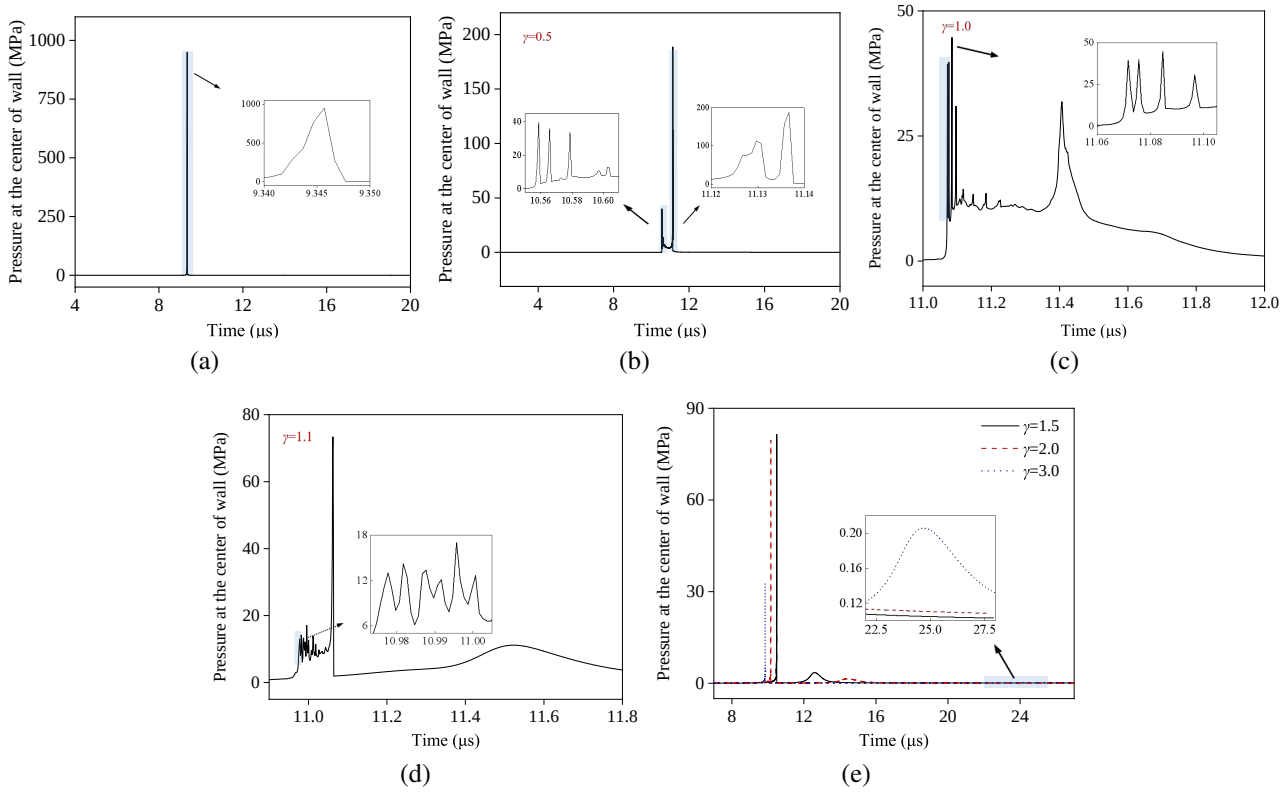

Fig. 8. Temporal evolution of central point pressure for different γ: (a) $\gamma = 0$, (b) $\gamma = 0.5$, (c) $\gamma = 1.0$, (d) $\gamma = 1.1$ and (e) $\gamma = 1.5$, 2.0, 3.0.

In Fig. 8(a), for $\gamma = 0$, a single peak pressure is observed between $t = 9.34$ μs and $t = 9.35$ μs. To identify its generation mechanisms, the distribution characteristics of pressure, velocity and bubble interface are discussed. In Fig. 9, for each sub-graph, the pressure field is represented on the left, and the velocity vector is shown on the right. The bubble interface is depicted by the blue solid line. In Fig. 9(a), the continuous collapse of the bubble results in an inward radial flow at $t = 9$ μs. As the shrinkage continues, the pressure inside the bubble steadily increases until complete collapse occurs. However, the fluid flow rate increases until $t = 9.344$ μs, as depicted in Fig. 9(d), and subsequently decreases. Importantly, no jet penetration occurs within the bubble, as illustrated in Fig. 9(f). Therefore, it can be concluded that the peak pressure of $\gamma = 0$ is caused by the shock wave release, and there is no micro-jet impacting the bottom wall throughout the process.

Fig. 8(b) depicts the pressure characteristics of the case $\gamma = 0.5$. The pressure peaks consist of two components. The

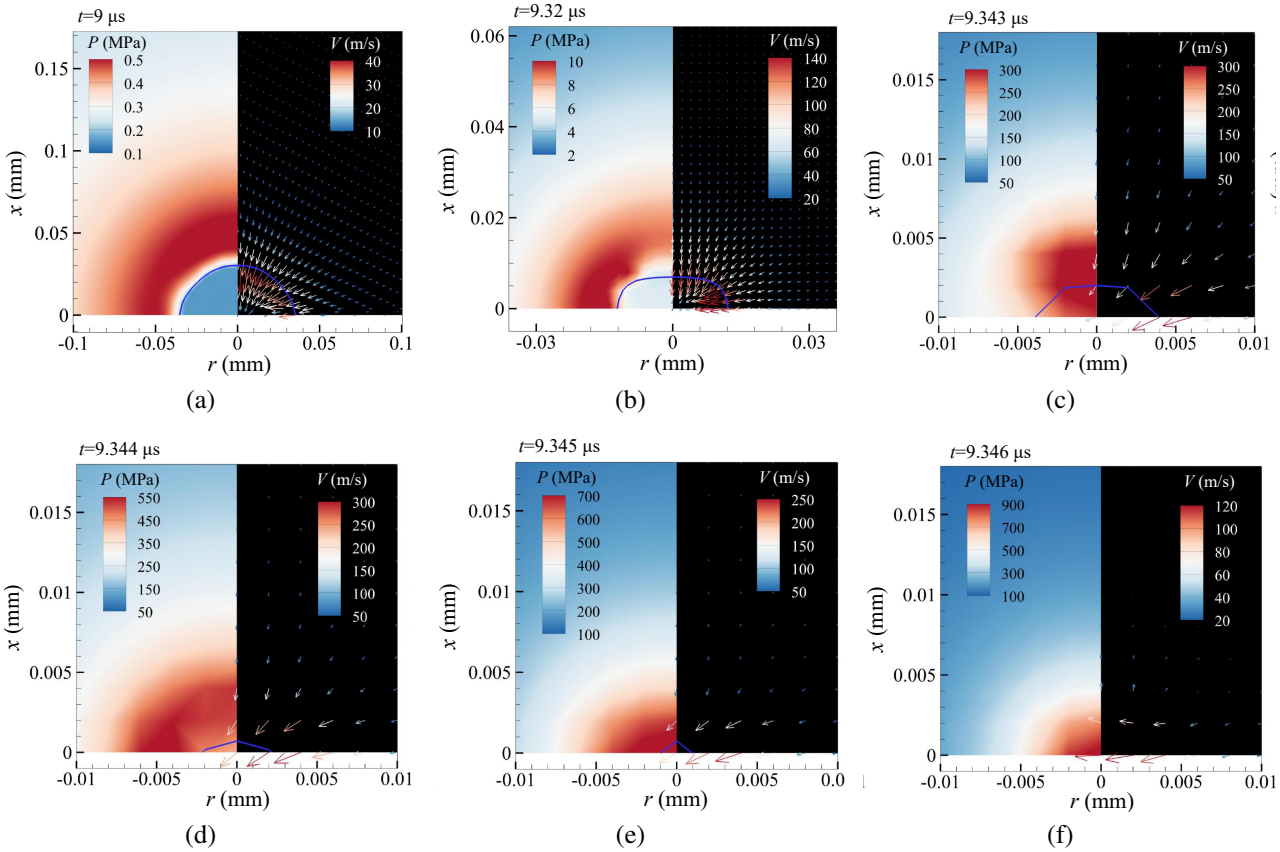

Fig. 9. Distribution of pressure, velocity and bubble interface for γ = 0: (a) t = 9 μs, (b) t = 9.32 μs, (c) t = 9.343 μs, (d) t = 9.344 μs, (e) t = 9.345 μs and (f) t = 9.346 μs.

peaks on the left side are smaller in magnitude but greater in quantity compared to those on the right side, and there exists a continuous impact effect on the wall between these two peaks. Fig. 10 presents the corresponding pressure, velocity vector, and bubble profiles. In Fig. 10(a), a high-pressure zone occurs at the upper bubble interface, causing the acceleration of the water between the high-pressure zone and the bubble interface. Consequently, at t = 9.45 μs, the upper bubble interface shrinks and becomes flattened. The velocity arrows located around the upper of bubble interface and exhibit perpendicular to the solid wall, which play a major role in penetrating inside the bubble. In Fig. 10(b), after penetrating the cavitation bubble completely, the jet directly impacts the solid wall at t = 10.56 μs. The first peak on the left side then generates, as illustrated in the pressure curve for γ = 0.5 in Fig. 8(b). Subsequently, the bubble shrinks under the compression of surrounding liquid and releases shock waves at the same time, leading to continuous impact towards the solid wall. In Fig. 10(c), the peak pressure observed at t = 10.566 μs further supports this observation. With further compression, the bubble divides into two smaller sub-bubbles at t = 11.04 μs, as depicted in Fig. 10(d). Simultaneously, the micro-jet changes direction radially upon impacting the solid wall and flows outward along the radial axis. Subsequently, in Figs. 10(e) and 10(f), these two sub-bubbles collapse at t = 11.13 μs and t = 11.137 μs, respectively. As a result, two intense shock waves are generated on the solid wall, corresponding to the two peak pressures observed on the right side of γ = 0.5 in Fig. 8(b). The shrinkage and collapse for the bubble of γ = 1.0 exhibits similar behaviours compared to the bubble of γ = 0.5.

As the value of γ increases to 1.1, depicted in Fig. 8(d), a sharp peak emerges with a brief duration. Subsequently, a long impact effect is exerted on the solid wall, resulting in a pronounced peak along the curve. Fig. 11 presents the corresponding temporal evolution of pressure, velocity vector, and bubble profile. In Fig. 11(a), at t = 9.96 μs, the generated micro-jet continues to propagate towards the bottom wall, while the toroidal bubble gradually shrinks under the compression of the surrounding fluid. In Figs. 11(c) and 11(d), it is evident that the high-pressure zone at the lower part of the bubble releases shock waves at t = 10.982 μs and t = 10.996 μs. This corresponds to the occurrence of small peaks in the pressure curve for γ = 1.1 in Fig. 8(d). In Fig. 11(e), the cavitation bubble collapses completely, generating intense shock waves at t = 11.063 μs, generating the prominent peak in the pressure curve shown in Fig. 8(d). Subsequently, the micro-jet impacts the wall, as shown in Fig. 11(f). Simultaneously, a vortex forms near the surface, as indicated by the vector arrows. When γ increases from 1.5 to 3.0, the pressure curves of these three cases exhibit a similar trend, featuring one prominent peak and one mound-like peak, as illustrated in Fig.

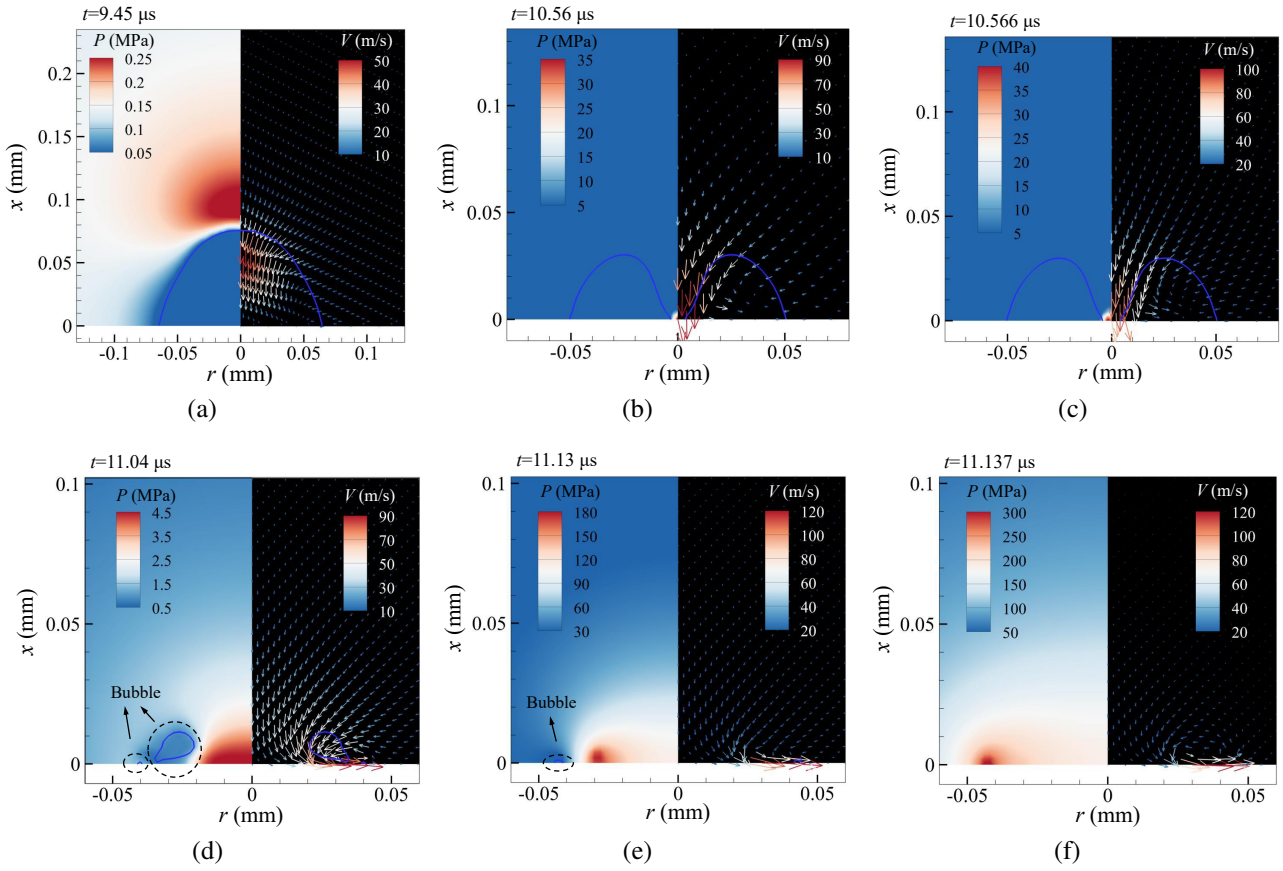

Fig. 10. Distribution of pressure, velocity and bubble interface for γ = 0.5: (a) t = 9.45 μs, (b) t = 10.56 μs, (c) t = 10.566 μs, (d) t = 11.04 μs, (e) t = 11.13 μs and (f) t = 11.137 μs.

8(e). The temporal evolution of bubble collapse characteristics at γ = 1.5, 2.0, and 3.0 closely resembles that observed for γ = 1.1.

The distribution of pressure on the solid wall for γ = 1.5 is shown in Fig. 12, and the moment corresponds to the state where peak pressures occur. It is evident that the shock wave sweeps across a significantly wider area, with an effective action radius on the wall reaching nearly 5 mm. This can result in circular corrosion pits with a severely eroded centre. The recalculated impact pressure induced by the micro-jet reaches up to 100 MPa, as presented in Table 1. The action radius of micro-jet is less than 50 μm, resulting in small spot corrosion pits.

The indicator point (x = 0.01 mm, r = 0 mm) is used to determine the impacting velocity of the micro-jet, as shown in Fig. 13. During the jet's approach to the wall, the velocity in all cases exhibits a fluctuating pattern with both upward and downward trends. For γ = 0, there are some details different from other cases. In Fig. 13(a), it is evident that the velocity for γ = 0 experiences a significant decline after t = 9.34 μs, followed by the emergence of a second peak velocity (Peak A) at t = 9.49 μs. This occurs due to the collision and merging of two jets moving in opposite directions, which then propagate radially away from the solid wall, as shown in Fig. 9(f). Subsequently, the merged jet passes through the indicator point, where the velocity is recorded once more, resulting in the appearance of Peak A.

Table 1. The shock wave pressure and jet impact pressure acting on the bottom wall.

γ	p_j	p_s	p_j/p_s
0	0	948.9	0
0.5	145.3	188.4	0.77
1.0	170.5	31.8	5.35
1.1	200.2	73.3	2.73
1.5	108.3	81.4	1.33
2.0	72.3	79.5	0.91
3.0	20.3	32.9	0.62

The pressure peak resulting from the impact of the jet is not substantial, as depicted in Fig. 8. Previous research (Xia et al., 2018) suggests that this lack of significant pressure peak may be attributed to the simulation's failure to account for the instantaneous, intense compression of the liquid upon jet-wall impact. Consequently, the jet impact pressure is recalculated utilizing the water-hammer principle (Cook and Parsons, 1928). The jet velocities employed are the maximum values

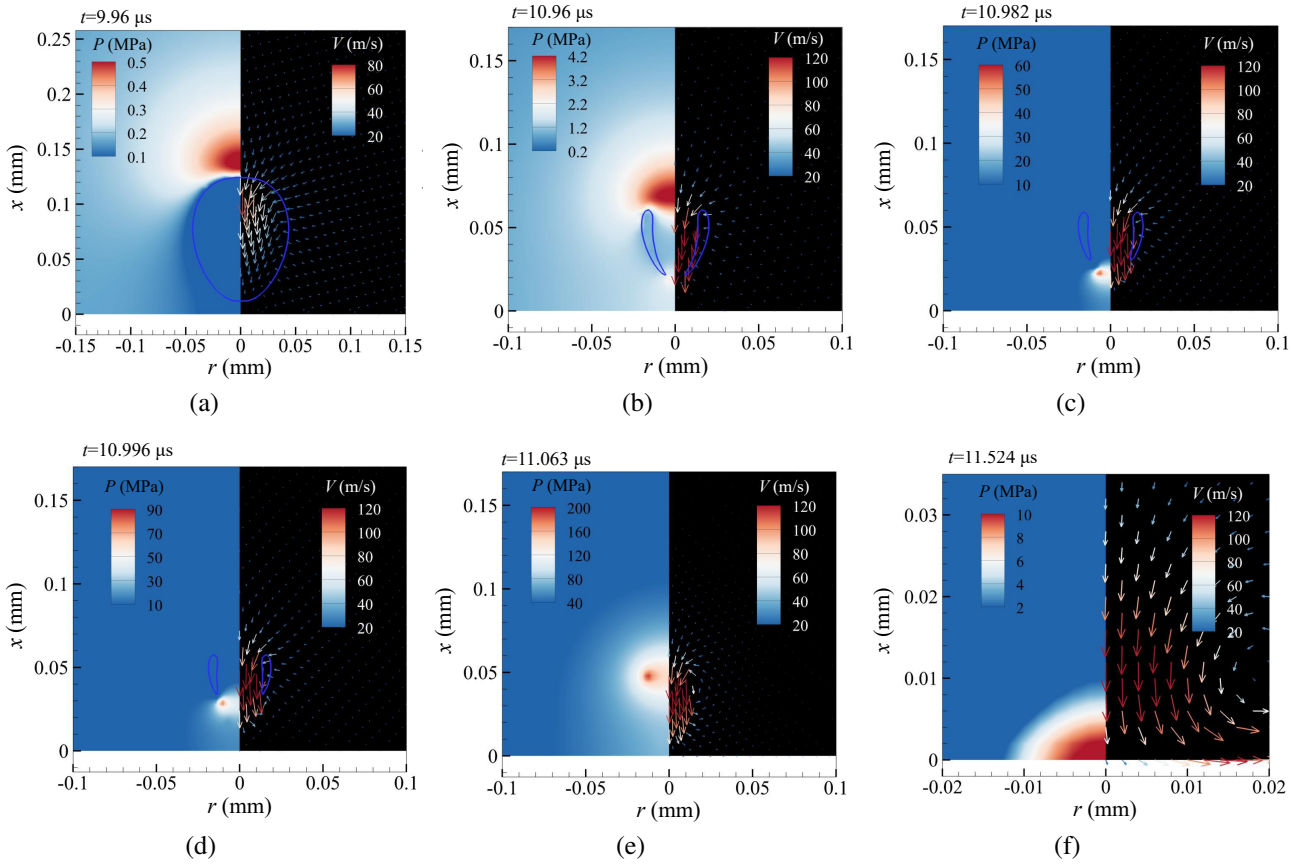

Fig. 11. Distribution of pressure, velocity and bubble interface for γ = 1.1: (a) t = 9.96 μs, (b) t = 10.96 μs, (c) t = 10.982 μs, (d) t = 10.996 μs, (e) t = 11.063 μs and (f) t = 11.524 μs.

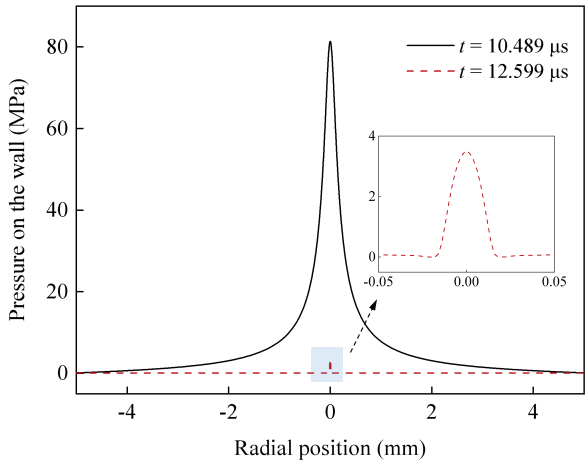

Fig. 12. The pressure distribution on the bottom wall for γ = 1.5.

obtained from Fig. 13. Table 1 presents a comparison of the shock wave pressure and jet impact pressure acting on the bottom wall. The ratio of p_j/p_s indicates that at γ = 0, 0.5 and 3.0, the shock wave contributes more in cavitation erosion process. Conversely, the micro-jet exhibits greater significance in cavitation damage at γ = 1.0 and 1.1. Furthermore, at γ = 1.5 and 2.0, the erosion intensity caused by the micro jet and shock wave is nearly equivalent.

5. Conclusion

The collapse behaviours of a single cavitation bubble with different stand-off distances are investigated. The temporal evolution of the bubble profile agrees well with experimental results, validating the accuracy of the current model. The main conclusions are as follows:

1) Cavitation bubbles exhibit two collapse patterns as γ varies from 0 to 3.0. For γ = 0, the bubble profile remains hemispherical and eventually collapses due to ambient pressure. For 0.5 $\leq \gamma \leq$ 3.0, the shrinkage of the bubble can be classified into the jet penetration stage and the collapse stage.
2) Increasing γ decreases the rate of bubble shrinkage and a delay in the collapse time when $\gamma \leq$ 1. Conversely, increasing γ leads to a more significant reduction in bubble volume and a decrease in the collapse time when $\gamma \geq$ 1.
3) Three cavitation erosion patterns are observed on the solid wall as γ varies from 0 to 3.0. For γ = 0, only the shock wave applies pressure to the bottom wall during the collapse. For γ = 0.5 and γ = 1.0, the jet penetrates inside the bubble and directly impacts it, followed by the shock wave generated by the bubble collapse acting on the solid wall. For γ = 1.1, 1.5, 2.0, and 3.0, the solid wall experiences the shock wave first and then the micro-jet

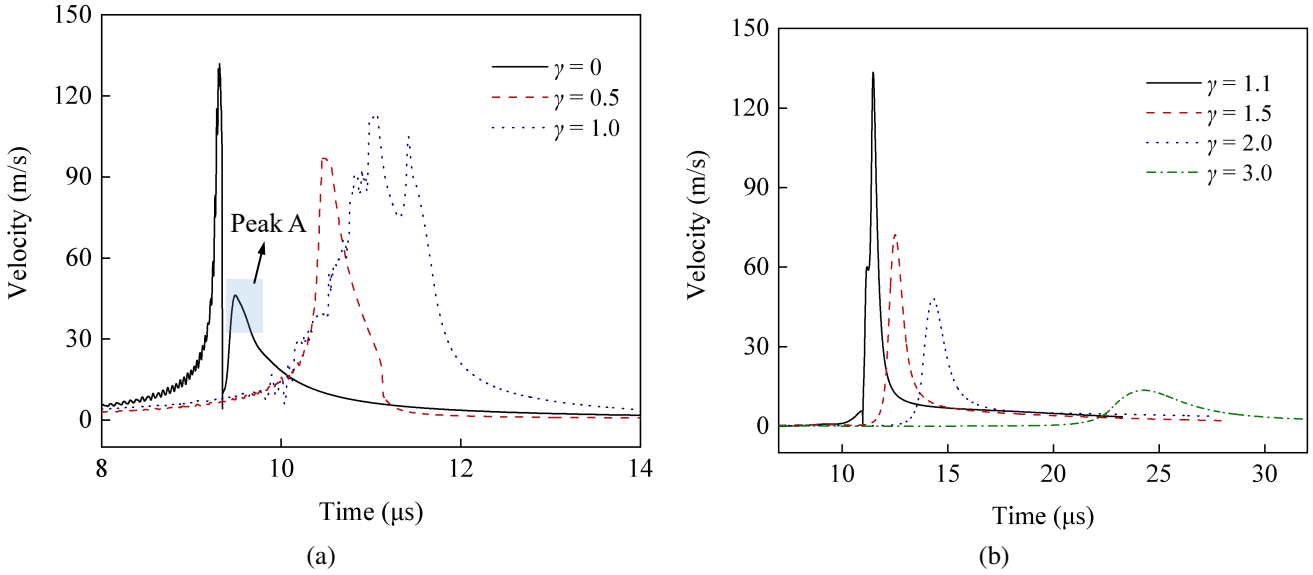

Fig. 13. The jet velocities at the indicator point (x = 0.01 mm, r = 0 mm) for different γ: (a) γ = 0, 0.5 and 1.0, (b) γ = 1.1, 1.5, 2.0 and 3.0.

impact.

4) In terms of cavitation damage, the shock wave has a greater contribution at γ = 0, 0.5, and 3.0, whereas the impact of the micro-jet is stronger at γ = 1.0 and 1.1. At γ = 1.5 and 2.0, the micro-jet and shock wave exhibit almost equivalent erosion intensity.
5) This study primarily investigates the generation mechanisms of the shock wave and micro-jet, and the precise prediction of cavitation damage remains undisclosed. The development of models for evaluating cavitation damage could be a potential avenue for future research.

Acknowledgements

This work was financially supported by National Natural Science Foundation of China (Nos. 52174009 and 51827804), Marine Economy Development Foundation of Guangdong Province (No. GDNRC[2022]44) “Technical Support for Stimulation and Testing of Gas Hydrate Reservoirs” and Scientific Research Foundation, China University of Petroleum (No. 462022YXZZ003).

Conflict of interest

The authors declare no competing interest.

References

Baliga, B. R., Patankar, S. V. A new finite-element formulation for convection-diffusion problems. Numerical Heat Transfer, 1980, 3(4): 393-409.

Brackbill, J. U., Kothe, D. B., Zemach, C. A continuum method for modeling surface tension. Journal of Computational Physics, 1992, 100(2): 335-354.

Brujan, E. A., Matsumoto, Y. Collapse of micrometer-sized cavitation bubbles near a rigid boundary. Microfluidics and Nanofluidics, 2012, 13(6): 957-966.

Bukharin, N., El Hassan, M., Omelyanyuk, M., et al. Applications of cavitating jets to radioactive scale cleaning in pipes. Energy Reports, 2020, 6: 1237-1243.

Cook, S. S., Parsons, C. A. Erosion by water-hammer. Proceedings of the Royal Society of London. Series A, Containing Papers of a Mathematical and Physical Character, 1928, 119(783): 481-488.

Cui, R., Li, S., Wang, S., et al. Pulsating bubbles dynamics near a concave surface. Ocean Engineering, 2022, 250: 110989.

Cui, Y., Lu, C., Wu, M., et al. Review of exploration and production technology of natural gas hydrate. Advances in Geo-Energy Research, 2018, 2(1): 53-62.

Hirt, C. W., Nichols, B. D. Volume of fluid (VOF) method for the dynamics of free boundaries. Journal of Computational Physics, 1981, 39(1): 201-225.

Huang, M., Su, D., Zhao, Z., et al. Numerical study of response behaviors of natural gas hydrate reservoir around wellbore induced by water jet slotting. Advances in Geo-Energy Research, 2023, 7(2): 75-89.

Issa, R. I. Solution of the implicitly discretised fluid flow equations by operator-splitting. Journal of Computational Physics, 1986, 62(1): 40-65.

Kornfeld, M., Suvorov, L. On the destructive action of cavitation. Journal of Applied Physics, 1944, 15(6): 495-506.

Lauterborn, W., Bolle, H. Experimental investigations of cavitation-bubble collapse in the neighbourhood of a solid boundary. Journal of Fluid Mechanics, 1975, 72(2): 391-399.

Li, G., Shen, Z., Zhou, C., et al. Investigation and application of self-resonating cavitating water jet in petroleum engi-

neering. Petroleum Science and Technology, 2005, 23(1): 1-15.

Li, G., Tian, S., Zhang, Y. Research progress on key technologies of natural gas hydrate exploitation by cavitation jet drilling of radial wells. Petroleum Science Bulletin, 2020, 5(3): 349-365. (in Chinese)

Minsier, V., Wilde, J. D., Proost, J. Simulation of the effect of viscosity on jet penetration into a single cavitating bubble. Journal of Applied Physics, 2009, 106(8): 084906.

Mohammad, P. F., Ehsan, R. Transient simulations of cavitating flows using a modified volume-of-fluid (VOF) technique. International Journal of Computational Fluid Dynamics, 2008, 22(1-2): 97-114.

Ohl, C. D., Arora, M., Dijkink, R., et al. Surface cleaning from laser-induced cavitation bubbles. Applied Physics Letters, 2006, 89(7): 074102.

Peng, C., Tian, S., Li, G. Joint experiments of cavitation jet: high-speed visualization and erosion test. Ocean Engineering, 2018, 149: 1-13.

Philipp, A., Lauterborn, W. Cavitation erosion by single laser-produced bubbles. Journal of Fluid Mechanics, 1998, 361: 75-116.

Plesset, M. S. The dynamics of cavitation bubbles. Journal of Applied Mechanics, 1949, 16(3): 277-282.

Rayleigh, L. VIII. On the pressure developed in a liquid during the collapse of a spherical cavity. The London, Edinburgh, and Dublin Philosophical Magazine and Journal of Science, 1917, 34(200): 94-98.

Shaibu, R., Sambo, C., Guo, B., et al. An assessment of methane gas production from natural gas hydrates: Challenges, technology and market outlook. Advances in Geo-Energy Research, 2021, 5(3): 318-332.

Soyama, H., Kikuchi, T., Nishikawa, M., et al. Introduction of compressive residual stress into stainless steel by employing a cavitating jet in air. Surface and Coatings Technology, 2011, 205(10): 3167-3174.

Thomson, G. W. The antoine equation for vapor-pressure data. Chemical Reviews, 1946, 38(1): 1-39.

Wang, G., Zhong, L., Zhou, S., et al. Jet breaking tools for natural gas hydrate exploitation and their support technologies. Natural Gas Industry B, 2018, 5(4): 312-318.

Wu, X., Zhang, Y., Tan, Y., et al. Flow-visualization and numerical investigation on the optimum design of cavitating jet nozzle. Petroleum Science, 2022, 19(5): 2284-2296.

Xia, D., Sun, C., Liu, Y., et al. Numerical simulation of micrometer-sized bubble collapse near a rigid boundary. Tribology, 2018, 38(6): 711-720.

Xu, W., Li, J., Luo, J., et al. Effect of a single air bubble on the collapse direction and collapse noise of a cavitation bubble. Experimental Thermal and Fluid Science, 2021, 120: 110218.

Yin, J., Zhang, Y., Zhu, J., et al. An experimental and numerical study on the dynamical behaviors of the rebound cavitation bubble near the solid wall. International Journal of Heat and Mass Transfer, 2021, 177: 121525.

Youngs, D. L. Numerical simulation of turbulent mixing by Rayleigh-Taylor instability. Physica D: Nonlinear Phenomena, 1984, 12(1): 32-44.

Zhang, Y., Wu, X., Zhao, S., et al. Numerical simulation of the straight-swirling integrated jet and its application in natural gas hydrate drilling. SPE Journal, 2022, 27(6): 3724-3739.

Zhou, S., Zhao, J., Li, Q., et al. Optimal design of the engineering parameters for the first global trial production of marine natural gas hydrates through solid fluidization. Natural Gas Industry B, 2018, 5(2): 118-131.